LETTER

https://doi.org/10.1038/s41586-018-0131-1

Rapid emergence of subaerial landmasses and onset of a modern hydrologic cycle 2.5 billion years ago

I. N. Bindeman[1]*, D. O. Zakharov[1], J. Palandri[1], N. D. Greber[2], N. Dauphas[3], G. J. Retallack[1], A. Hofmann[4], J. S. Lackey[5] & A. Bekker[4,6]

The history of the growth of continental crust is uncertain, and several different models that involve a gradual, decelerating, or stepwise process have been proposed[1–4]. Even more uncertain is the timing and the secular trend of the emergence of most landmasses above the sea (subaerial landmasses), with estimates ranging from about one billion to three billion years ago[5–7]. The area of emerged crust influences global climate feedbacks and the supply of nutrients to the oceans[8], and therefore connects Earth's crustal evolution to surface environmental conditions[9–11]. Here we use the triple-oxygen-isotope composition of shales from all continents, spanning 3.7 billion years, to provide constraints on the emergence of continents over time. Our measurements show a stepwise total decrease of 0.08 per mille in the average triple-oxygen-isotope value of shales across the Archaean–Proterozoic boundary. We suggest that our data are best explained by a shift in the nature of water–rock interactions, from near-coastal in the Archaean era to predominantly continental in the Proterozoic, accompanied by a decrease in average surface temperatures. We propose that this shift may have coincided with the onset of a modern hydrological cycle owing to the rapid emergence of continental crust with near-modern average elevation and aerial extent roughly 2.5 billion years ago.

Changes in Earth's surface environments between about 2.5 billion years ago (2.5 Gyr ago) and 2.32 Gyr ago are recorded in numerous isotopic and elemental systems, which point to a dramatic change in the oxygenation of the atmosphere and oceans at that time[9,10]. These changes were associated with a series of three to four 'Snowball Earth' glaciations[11,12], whose origin and driving forces are still debated. The major geochemical and biogeochemical rearrangements in Earth's surface environments at the Archaean–Proterozoic boundary (2.5 Gyr ago) also left numerous signatures in the geological record. Among these signatures is a steep rise in the oxygen isotopic $^{18}O/^{16}O$ ratio (expressed as $\delta^{18}O$, the deviation in the ratio in per mille relative to the standard ratio in modern seawater, VSMOW) of shales and zircons in the Late Archaean, followed by a progressively decelerating increase in these values into the Phanerozoic[13,14]. This first-order trend was modulated by the assembly and break-up of supercontinents[14]. However, it is unclear how these changes in $\delta^{18}O$ (as well as other parameters) relate to the isotopic evolution of continental crust, to the evolution of meteoric water, or to weathering conditions at Earth's surface.

We present here triple-oxygen-isotope measurements of shales, which are the dominant sedimentary rocks on Earth and the products of the chemical and physical weathering of landmasses that are exposed to the atmosphere. Shales consist mainly of clay minerals, secondary quartz and unmodified detrital minerals; studies of shales have been used previously to constrain the chemical evolution of Earth's crust through time[1,3,8,15,16]. The triple-oxygen-isotope composition of shales is expressed here as $\delta'^{18}O$ and $\Delta'^{17}O$ values; the latter parameter reflects linearized deviations in per mille (‰) of $^{17}O/^{16}O$ ratios relative to a mass-dependent $^{17}O/^{16}O$ versus $^{18}O/^{16}O$ fractionation line with a reference slope of 0.5305 (see Fig. 1 and Supplementary Information section 'Methods' for details). Both parameters are independent functions of temperature and oxygen-isotope variations and fractionation processes in surface environments[17–19].

The $\delta'^{18}O$–$\Delta'^{17}O$ signature of bulk shales is defined by: first, the proportions of detrital versus authigenic mineral components; second, the temperature of weathering and diagenesis, which affects isotopic fractionation factors; and third, the isotopic composition of the altering water (Fig. 1). Although used extensively in the past, $^{18}O/^{16}O$ ratios alone[14,20,21] are insufficient for disentangling the impact of these various processes on the shale composition. However, as we show here, the combined use of $\delta'^{18}O$ and $\Delta'^{17}O$ removes the ambiguities associated with using $\delta'^{18}O$ alone, and allows us to reconstruct past surface conditions and the composition of meteoric waters involved in weathering.

The shale samples used here are the same as those used previously[14], with the addition of 30 composite samples (formation-averaged) and 10 individual recent and Archaean samples (Fig. 1, Extended Data Tables 1–3). These 278 samples were collected from outcrops and drill holes on all continents and span 3.7 Gyr. The measured $\delta^{18}O$ values agree with previously determined values for shales and other sediment types and detrital zircons (Fig. 2)[7,13,14,16]. The bulk shales cover a large field in the $\delta'^{18}O$–$\Delta'^{17}O$ space (Fig. 1). The observed $\Delta'^{17}O$ values range from those typical of mantle and crust (−0.05‰ to −0.09‰)[18,22] to −0.3‰. Furthermore, the triple-oxygen-isotope data of shales fall on different mass-dependent fractionation lines, with slopes between the $^{18}O/^{16}O$ and $^{17}O/^{16}O$ ratios ranging from 0.529 to 0.516 (Fig. 1, Supplementary Information)—values that encompass the entire range of slopes described previously for mass-dependent processes on Earth[22].

Our results confirm a gradual trend of increasing $\delta'^{18}O$ values from 3.7 Gyr ago towards modern times. Meanwhile, the $\Delta'^{17}O$ values of shales exhibit a stepwise shift to more negative and more diverse values during and after the Archaean–Proterozoic transition (Fig. 2a). Shales older than 2.5 Gyr define an average $\Delta'^{17}O$ value of $-0.047‰ \pm 0.012‰$ ($\pm 2\sigma$), while shales younger than 2.2 Gyr—deposited in later stages and after the Great Oxidation Event (GOE) roughly 2.32 Gyr ago, during which O_2 appeared in the atmosphere—yield an average $\Delta'^{17}O$ value of $-0.118‰ \pm 0.024‰$. This difference in the triple-oxygen-isotope composition of the two age groups cannot be explained solely by different equilibration temperatures, or by the mixing of different proportions of variably weathered detrital materials, as the shale record cuts across the $\delta'^{18}O$–$\Delta'^{17}O$ trends defined by these processes (Fig. 1), requiring different initial $\delta'^{18}O$ meteoric waters. Moreover, there is no difference in the chemical index of alteration (CIA[23]) or in the proportions of minerals (determined by X-ray diffraction, XRD) of the studied shales across the GOE (Extended Data Table 2, Fig. 2) that could explain the observed shift in the $\Delta'^{17}O$ values of the shales. The invariable titanium-isotope values[8] and constant characteristic elemental ratios of the studied shales[14] (Extended Data Fig. 1) suggest that

[1]Department of Earth Sciences, University of Oregon, Eugene, OR, USA. [2]Department of Earth Sciences, University of Geneva, Geneva, Switzerland. [3]Origins Laboratory, Department of the Geophysical Sciences and Enrico Fermi Institute, The University of Chicago, Chicago, IL, USA. [4]Department of Geology, University of Johannesburg, Auckland Park, South Africa. [5]Department of Geology, Pomona College, Claremont, CA, USA. [6]Department of Earth Sciences, University of California, Riverside, CA, USA. *e-mail: bindeman@uoregon.edu

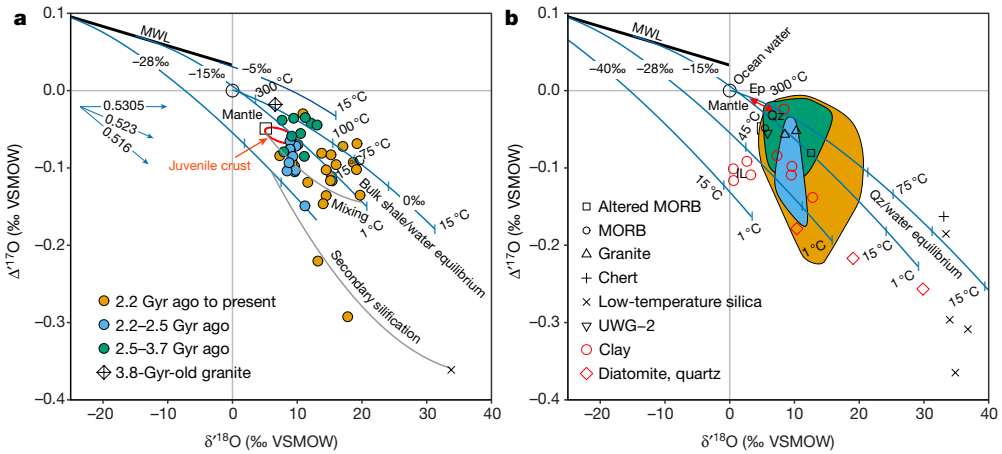

Fig. 1 | Triple-oxygen-isotope systematics of ancient and modern terrestrial materials. a, Ancient materials. **b**, Modern materials. The coloured fields in **b** correspond to the ancient-shale data shown with coloured dots in **a**. The concave blue curves represent isotopic fractionation between weathering products and meteoric water. The labels on the blue curves show the $\delta'^{18}O$ values of meteoric waters, ranging from −5‰ to −40‰, and of modern ocean water (black open circle; 0‰). The modern meteoric water line is labelled MWL. In **a**, the fractionation curves for bulk shale/water equilibration were constructed assuming a weathering product of 70% illite and 30% quartz (see Supplementary Information). In **b**, the fractionation curves are based on experimentally determined quartz/water triple-oxygen-isotope fractionations[19]. In **a**, the grey convex mixing curve connects unweathered terrestrial materials (such as mantle or upper crust) with the weathering products located on the blue fractionation lines; the grey secondary silicification curve connects modern high-$\delta'^{18}O$ and low-$\Delta'^{17}O$ materials (such as cherts and sponge spicules; individual data are shown in **b**). In **b**, the various Earth materials analysed here (red symbols) and in refs[18,19] (black symbols) are normalized to a mantle $\Delta'^{17}O$ value of −0.05‰; the double-headed red arrow, with a slope of 0.528, connects coexisting hydrothermal quartz (Qz) and epidote (Ep) from the modern deep-ocean core 504B, which formed at about 300 °C in equilibrium with roughly 0‰ seawater. In **a**, the blue arrows and associated values depict the slopes of triple-oxygen fractionation in linearized $\delta'^{17}O$–$\delta'^{18}O$ space, with the values reflecting logarithmic linearization of the delta scales[32] (see Supplementary Information); 0.5305 is characteristic of infinitely high temperatures and smaller slopes are characteristic of lower-temperature fractionations. IL, illite; VSMOW, Vienna Standard Mean Ocean Water.

the parental, atmospherically exposed continental crust undergoing weathering was similar in chemical composition to the modern crust, and has had similar proportions of mafic and felsic rocks since at least 3.5 Gyr ago, with a greater contribution of komatiites in the Archaean[8,16]. Higher-temperature Archaean oceans[24], or a greater contribution of hydrothermal clays to Archaean shales, would result in less-positive $\delta'^{18}O$ and less-negative $\Delta'^{17}O$ values. Although this could help to explain the lower $\delta'^{18}O$ values that we observe[24], it cannot explain the vertically extending trend of lower $\Delta'^{17}O$ values (Fig. 1, Extended Data Fig. 2) or the step change in $\Delta'^{17}O$ values 2.5 Gyr ago (Fig. 2). In addition, our shales show no geological or mineralogical evidence for a substantial change in hydrothermal contribution or weathering intensity in the CIA parameter across the Archaean–Proterozoic boundary[14]. Taking a cue from the modern world, where meteoric water shows variable $\delta'^{18}O$–$\Delta'^{17}O$ compositions[17], the simplest explanation for some of the oxygen-isotope variations measured in ancient shales is that they were in part inherited from the waters involved in rock alteration on the continents.

We applied recently established isotope-fractionation factors for $^{18}O/^{16}O$ and $^{17}O/^{16}O$ between quartz and water at different temperatures[19] to transform our measured, raw $\delta'^{18}O$–$\Delta'^{17}O$ data for shales into actual surface weathering conditions. We also calculated the equilibrium fractionation of oxygen isotopes between bulk shale and water, at different temperatures and initial $\delta'^{18}O$–$\Delta'^{17}O$ water values along the meteoric water line (MWL; Fig. 1, Extended Data Figs. 3–5). Oxygen-isotope fractionation between clay minerals and water under low temperatures is less than that for water and secondary quartz[20], but the two mineral/water pairs follow the same fractionation law (ref. [18]; see also Supplementary Information and Extended Data Fig. 6). The bulk shale/water fractionation lines (blue curves in Fig. 1a) define a negative slope in $\delta'^{18}O$–$\Delta'^{17}O$ space. Mixing detrital material derived from the continental crust with authigenic minerals follows a subparallel curve (grey line in Fig. 1a) within the field defined by the isotope-fractionation curves. The calculation shows that variations in temperature, in the initial oxygen-isotope composition of altering waters, and in mixing ratios between detrital material and weathering products can explain the overall trend and negative co-variations in our data.

The proportion of weathering products in a shale can be assessed independently via its mineralogical composition (through XRD) and/or its chemical composition (such as through the CIA[23]). Combining this estimate with the $\delta'^{18}O$ and $\Delta'^{17}O$ values of the shales and the pristine detrital components (igneous rocks) allows us to calculate, by mass balance, the $\delta'^{18}O$ and $\Delta'^{17}O$ values of the weathering products (Extended Data Fig. 3). The CIA index has remained nearly constant through time[14] (Extended Data Fig. 7), suggesting that a secular trend in weathering intensity is unlikely to introduce a systematic bias in this approach. The equations for isotopic fractionation during water–rock interactions and the equation of the MWL in $\delta'^{18}O$–$\Delta'^{17}O$ space (Fig. 1) can be used to independently calculate the water–rock interaction temperature and the oxygen-isotopic composition ($\delta'^{18}O_W$ and $\Delta'^{17}O_W$) of waters involved in weathering and diagenesis (Extended Data Figs. 3, 4). This approach is likely to be oversimplified, because detrital components in shale precursors were probably altered by a range of meteoric and diagenetic waters at different temperatures in watersheds. But, given that we compare shales with shales, all of which have comparable CIAs, these complexities do not affect the first-order interpretations afforded by quantitative modelling.

We find that the temperatures of interacting water and rock derived from the inversion of shale $\delta'^{18}O$–$\Delta'^{17}O$ values were higher during the Archaean than after it (Extended Data Fig. 5). This modelling exercise also shows that—although our measurements reveal trends towards heavier average $\delta'^{18}O$ and lighter average $\Delta'^{17}O$ values in shales over time—the waters involved in surface alteration and weathering processes became lighter in $\delta'^{18}O$, heavier in $\Delta'^{17}O$, and more variable in both $\delta'^{18}O$ and $\Delta'^{17}O$ after roughly 2.5 Gyr ago. Although the quantitative analysis makes important simplifications, it does capture the essential features of weathering conditions on continents through time.

Another explanation for the stepwise change in $\Delta'^{17}O$ values during the GOE could be the appearance of atmospheric oxygen and ozone.

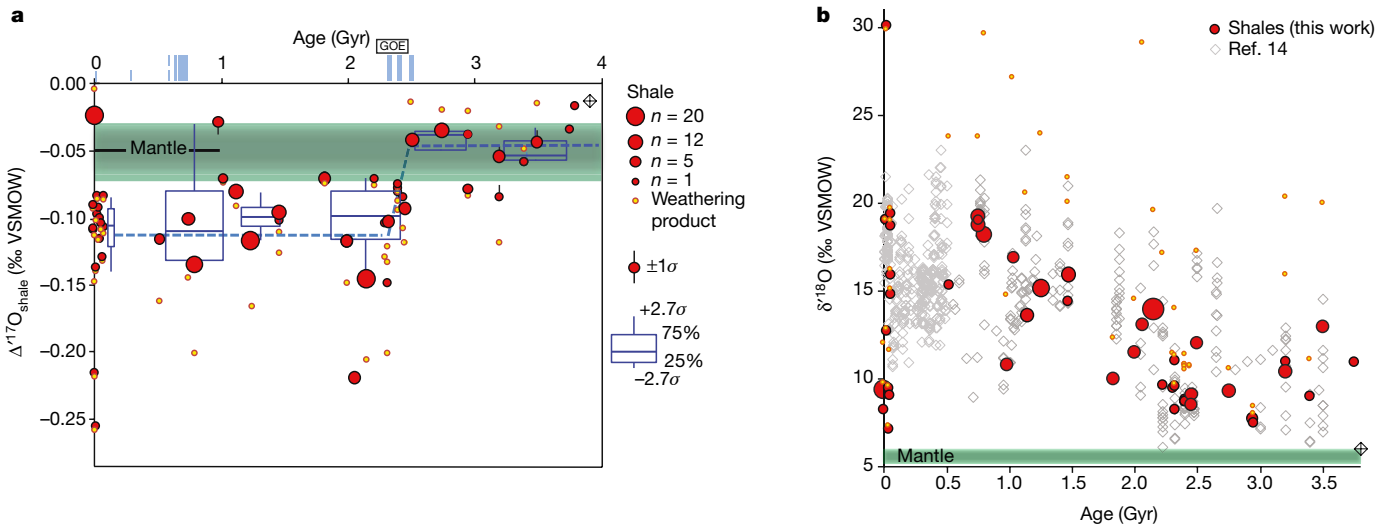

Fig. 2 | Oxygen-isotopic compositions of shales through time. a, $\Delta'^{17}O$ record of shales (red points) and calculated oxygen-isotopic composition of weathering products (yellow points), showing a stepwise change in composition between 2.5 Gyr ago and 2.2 Gyr ago. The blue dashed lines represent the mean $\Delta'^{17}O$ values, weighted by the composite sample size (n), for shales before 2.5 Gyr ago and after 2.2 Gyr ago. The boxes represent the medians, interquartile ranges and extreme values (see legend). A t-test reveals that the Archaean and post-Archaean $\Delta'^{17}O$ values are statistically distinct ($0.004 < P < 0.02$, well below a statistical significance value of 0.05). We attribute the different $\delta'^{18}O$ and $\Delta'^{17}O$ values of pre- and post-Archaean shales in this diagram to a change from a coast-dominated to a more continental hydrological cycle and weathering conditions (see text for details). The blue vertical bars at the top indicate major glacial episodes. **b**, $\delta'^{18}O$ record of shales (red points) from our dataset superimposed on the dataset from ref. [14] (white diamonds).

The formation of ozone with highly positive $\Delta'^{17}O$ values (+30‰ to +100‰) via ultraviolet photolysis in the stratosphere leaves atmospheric oxygen with the slightly negative $\Delta'^{17}O$ value of −0.3‰ in today's 21 vol% oxygen atmosphere[22,25], but probably much less in Proterozoic conditions of less than 1 vol% oxygen. However, not only was the atmospheric $\Delta'^{17}O$ signal small, there is also no mechanism by which to transfer this signature into the meteoric water cycle and hence into crustal silicate weathering products such as shales.

As argued above, we favour an explanation by which the difference in the $\Delta'^{17}O$ values of pre- and post-GOE shales occurred through a change in the meteoric water cycle (Fig. 3). Starting roughly at the Archaean–Proterozoic transition, the emerged crust would have interacted with waters that had more variable and on average more negative $\delta'^{18}O_W$ values and more positive $\Delta'^{17}O_W$ values than before the GOE (with $\Delta'^{17}O_W$ shifted by approximately +0.1‰). The observed shift in the triple-oxygen-isotope composition of shales would also have required lower post-GOE surface temperatures (Extended Data Fig. 5). This is broadly consistent with the findings of previous studies of $\delta'^{18}O$ values in cherts[24].

In the modern world, the oxygen-isotope composition of precipitation depends on the cumulative history of water loss from the air parcel that is travelling inland away from the coasts towards higher latitudes and higher altitudes (http://www.waterisotopes.org), resulting in lower $\delta'^{18}O_W$ values, higher $\Delta'^{17}O_W$ values, and more diverse compositions overall[17] (as in the MWL on Fig. 1). This combined effect, which we call 'continentality' (Fig. 3), is shown through the shale record's step change that coincides with the Archaean–Proterozoic boundary (Figs. 2a, 3). It is most likely that the observed change in the shale triple-oxygen-isotope record reflects the appearance of larger continents (Fig. 3) and higher elevations from the Proterozoic onwards—a period that is broadly contemporaneous with the final stages in the assembly of the first documented supercontinent, Kenorland[2,26], or with the formation of several supercratons[12,15] immediately before the GOE[27]. Supercontinent assembly and orogenic events result in high mountain ranges and plateaus, as occurred when India collided with Asia, forming the Himalayas and Tibet. Rising mountains in even quite low to mid latitudes result in precipitation with very light $\delta'^{18}O$ values (http://www.waterisotopes.org) that correlate with elevation, with a roughly 2‰–3‰ drop in $\delta'^{18}O$ per kilometre of altitude gain[28].

Supporting our interpretations of triple-oxygen variations in shales is the strontium-isotope record of marine carbonates, which suggests

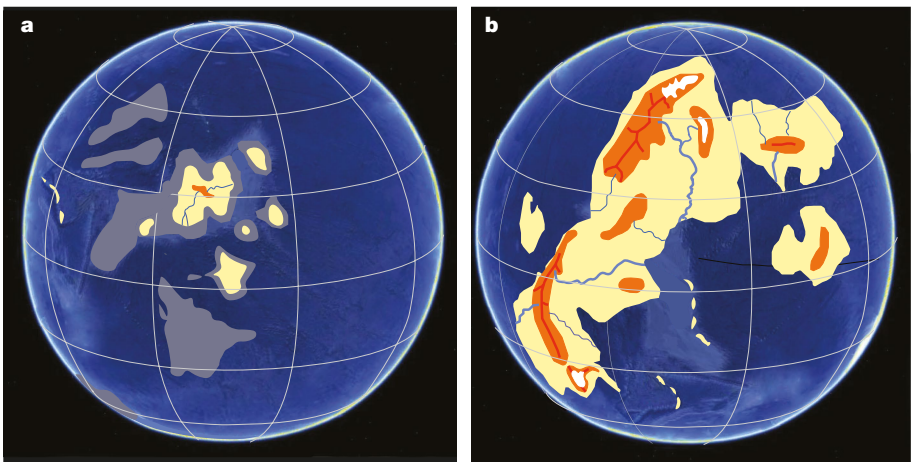

Fig. 3 | Conceptual palaeohypsometry of Archean and Proterozoic worlds. These images are based on palaeomagnetic and tectonic reconstructions (see refs [12,26] and references therein). **a**, The late Archaean era (shortly before 2.5 Gyr ago) during the assembly of the supercontinent Kenorland. **b**, The early/mid Paleoproterozoic era, after the occurrence of the GOE. The oceans are shallower in **a** compared with **b**, and the (excessively flooded) continents are smaller and lower, resulting in different hydrologic and weathering cycles, as described here.

that the area of emerged continental crust increased substantially and irreversibly at roughly the Archaean–Proterozoic boundary[29]. From a geodynamic perspective, models of a cooling Earth call for a thickening of the lithosphere and the establishment of a higher continental freeboard by about 2.5 Gyr ago owing to increased mantle viscosity[5,30,31]. The emergence of large landmasses (Fig. 3) would also have led to a larger weathering sink for carbon dioxide, which occurred at greater concentrations in the Archaean, resulting in a transition to moderate surface temperatures after the GOE. We conclude that this set of large-scale tectonic and near-surface changes best explains the observed shift in the $\delta'^{18}O$–$\Delta'^{17}O$ composition of shales between 2.5 Gyr ago and 2.2 Gyr ago (Fig. 2).

The rapid increase in Earth's subaerial surface and overall hypsometry 2.5 Gyr ago that we infer here (Fig. 3) would have also increased Earth's albedo, the flux of nutrients to the oceans[8] from continents undergoing subaerial weathering, and the extent of continental margins, additionally resulting in a higher rate of burial of organic carbon and reducing the concentration of carbon dioxide in the air. Together, these changes could have contributed to the cooling of the planet and to the snowball glaciations of the early Palaeoproterozoic, followed by the GOE, highlighting how Earth's interior could have influenced surface redox conditions and chemistry. The most dramatic change in Earth's history was marked by a transition from hot and largely anoxic surface conditions to an oxygenated atmosphere with moderate surface temperatures. Our study suggests that this transition might have been modulated by long-term cooling of the subcontinental mantle and lithosphere, rendering it capable of supporting a thicker crust[1,2,30,31]. This would have led to the emergence of extensive landmasses at the Archaean–Proterozoic boundary, with life and surface conditions adjusting to—rather than triggering—the change in atmospheric oxygen concentrations.

Data availability

Data are provided in Extended Data Tables 1–3.

Online content

Any Methods, including any statements of data availability and Nature Research reporting summaries, along with any additional references and Source Data files, are available in the online version of the paper at https://doi.org/10.1038/s41586-018-0131-1.

Received: 2 October 2017; Accepted: 7 March 2018;
Published online 23 May 2018.

1. Taylor, S. R. & McLennan, S. M. The geochemical evolution of the continental crust. *Rev. Geophys.* **33**, 241–265 (1995).
2. Condie, K. C. *Plate Tectonics and Crustal Evolution* 3rd edn (Pergamon Press, Oxford, 2013).
3. Belousova, E. A. et al. The growth of the continental crust: constraints from zircon Hf-isotope data. *Lithos* **119**, 457–466 (2010).
4. Keller, C. B., Schoene, B., Barboni, M., Samperton, K. M. & Husson, J. M. Volcanic–plutonic parity and the differentiation of the continental crust. *Nature* **523**, 301–307 (2015).
5. Dhuime, B., Wuestefeld, B. & Hawkesworth, C. J. Emergence of modern continental crust about 3 billion years ago. *Nat. Geosci.* **8**, 552–555 (2015).
6. Lee, C.-T. A. et al. Deep mantle roots and continental emergence: implications for whole-Earth elemental cycling, long-term climate, and the Cambrian explosion. *Int. Geol. Rev.* **60**, 431–448 (2017).
7. Hawkesworth, C. J., Cawood, P. A., Dhuime, B. & Kemp, A. I. S. Earth's continental lithosphere through time. *Annu. Rev. Earth Planet. Sci.* **45**, 169–198 (2017).
8. Greber, N. D. et al. Titanium isotopic evidence for felsic crust and plate tectonics 3.5 billion years ago. *Science* **357**, 1271–1274 (2017).
9. Farquhar, J. & Wing, B. A. The terrestrial record of stable sulphur isotopes: a review of the implications for evolution of Earth's sulphur cycle. *Geol. Soc. Lond. Spec. Publ.* **248**, 167–177 (2005).
10. Bekker, A. et al. Dating the rise of atmospheric oxygen. *Nature* **427**, 117–120 (2004).
11. Hoffman, P. F. The Great Oxidation and a Siderian snowball Earth: MIFS based correlation of Paleoproterozoic glacial epochs. *Chem. Geol.* **362**, 143–156 (2013).
12. Gumsley, A. P. et al. Timing and tempo of the Great Oxidation Event. *Proc. Natl Acad. Sci. USA* **114**, 1811–1816 (2017).
13. Valley, J. W. et al. 4.4 billion years of crustal maturation: oxygen isotope ratios of magmatic zircon. *Contrib. Mineral. Petrol.* **150**, 561–580 (2005).
14. Bindeman, I. N., Bekker, A. & Zakharov, D. O. Oxygen isotope perspective on crustal evolution on early Earth: a record of Precambrian shales with emphasis on Paleoproterozoic glaciations and Great Oxygenation Event. *Earth Planet. Sci. Lett.* **437**, 101–113 (2016).
15. Bleeker, W. The late Archean record: a puzzle in ca. 35 pieces. *Lithos* **71**, 99–134 (2003).
16. Gaschnig, R. M. et al. Compositional evolution of the upper continental crust through time, as constrained by ancient glacial diamictites. *Geochim. Cosmochim. Acta* **186**, 316–343 (2016).
17. Luz, B. & Barkan, E. Variations of $^{17}O/^{16}O$ and $^{18}O/^{16}O$ in meteoric waters. *Geochim. Cosmochim. Acta* **74**, 6276–6286 (2010).
18. Pack, A. & Herwartz, D. The triple oxygen isotope composition of the Earth mantle and understanding $\delta^{17}O$ variations in terrestrial rocks and minerals. *Earth Planet. Sci. Lett.* **390**, 138–145 (2014).
19. Sharp, Z. D. et al. A calibration of the triple oxygen isotope fractionation in the SiO_2-H_2O system and applications to natural samples. *Geochim. Cosmochim. Acta* **186**, 105–119 (2016).
20. Savin, S. & Epstein, S. The oxygen and hydrogen isotope geochemistry of ocean sediments and shales. *Geochim. Cosmochim. Acta* **34**, 43–63 (1970).
21. Land, L. S. & Lynch, F. L. $\delta^{18}O$ values of mudrocks: more evidence for an ^{18}O-buffered ocean. *Geochim. Cosmochim. Acta* **60**, 3347–3352 (1996).
22. Bao, H. M., Cao, X. B. & Hayles, J. Triple-oxygen isotopes: fundamental relationships and applications. *Annu. Rev. Earth Planet. Sci.* **44**, 463–492 (2016).
23. Nesbitt, H. W. & Young, G. N. Early Proterozoic climates and plate motions inferred from major element chemistry of lutites. *Nature* **299**, 715–717 (1982).
24. Knauth, L. P. & Lowe, D. R. High Archean climatic temperature inferred from oxygen isotope geochemistry of cherts in the 3.5 Ga Swaziland Supergroup, South Africa. *Geol. Soc. Bull.* **115**, 566–580 (2003).
25. Young, E., Yeung, L. Y. & Kohl, I. On the ^{17}O budget of atmosphere. *Geochim. Cosmochim. Acta* **135**, 102–125 (2014).
26. Mertanen, S. & Pesonen, L. J. in *From the Earth's Core to Outer Space* (ed. Haapala, I.) 11–35 (Springer, Berlin, 2012).
27. Barley, M. E., Bekker, A. & Krapez, B. Late Archean to early Paleoproterozoic global tectonics, environmental change and the rise of atmospheric oxygen. *Earth Planet. Sci. Lett.* **238**, 156–171 (2005).
28. Rowley, D. B., Pierrehumbert, R. & Currie, B. A new approach to stable isotope-based paleoaltimetry: implications for paleoaltimetry and paleohypsometry of the High Himalaya since the Late Miocene. *Earth Planet. Sci. Lett.* **188**, 253–268 (2001).
29. Flament, N., Coltice, N. & Rey, P. F. A case for late-Archaean continental emergence from thermal evolution models and hypsometry. *Earth Planet. Sci. Lett.* **275**, 326–336 (2008).
30. Vlaar, N. J. Continental emergence and growth on a cooling earth. *Tectonophysics* **322**, 191–202 (2000).
31. Korenaga, J., Planavsky, N. J. & Evans, D. A. D. Global water cycle and the coevolution of the Earth's interior and surface environment. *Phil. Trans. R. Soc. A* **375**, 20150393 (2017).
32. Miller, M. F. Isotopic fractionation and the quantification of ^{17}O anomalies in the oxygen three-isotope system: an appraisal and geochemical significance. *Geochim. Cosmochim. Acta* **66**, 1881–1889 (2002).

Acknowledgements This work was supported by National Science Foundation (NSF) grant EAR1447337 and by the University of Oregon. N.D. was supported by NSF grant EAR1502591. A.B. was supported by National Sciences and Engineering Research Council (NSERC) Discovery and Accelerator grants. We thank P. Hoffman, S. Mertanen and D. Evans for discussions about Precambrian palaeogeography and environmental changes; K. Johnson for technical help with vacuum lines; and O. Melnik for help with programming.

Reviewer information *Nature* thanks C. Hawkesworth and the other anonymous reviewer(s) for their contribution to the peer review of this work.

Author contributions I.N.B. conceived the study and wrote the paper; D.O.Z., J.P. and I.N.B. built the purification line and collected the data; N.D.G. and N.D. provided composite shale samples studied previously for titanium isotopes; A.B., A.H. and G.J.R. provided samples; J.S.L. performed major- and trace-element analyses; I.N.B. and N.D. discussed the inversion approach and I.N.B. implemented the model; D.O.Z. contributed to statistical treatment; A.B., N.D., N.D.G. and G.J.R. contributed to discussions on Precambrian environments and crustal evolution. All authors contributed to writing and editing the paper.

Competing interests The authors declare no competing interests.

Additional information
Extended data is available for this paper at https://doi.org/10.1038/s41586-018-0131-1.
Supplementary information is available for this paper at https://doi.org/10.1038/s41586-018-0131-1.
Reprints and permissions information is available at http://www.nature.com/reprints.
Correspondence and requests for materials should be addressed to I.N.B.
Publisher's note: Springer Nature remains neutral with regard to jurisdictional claims in published maps and institutional affiliations.

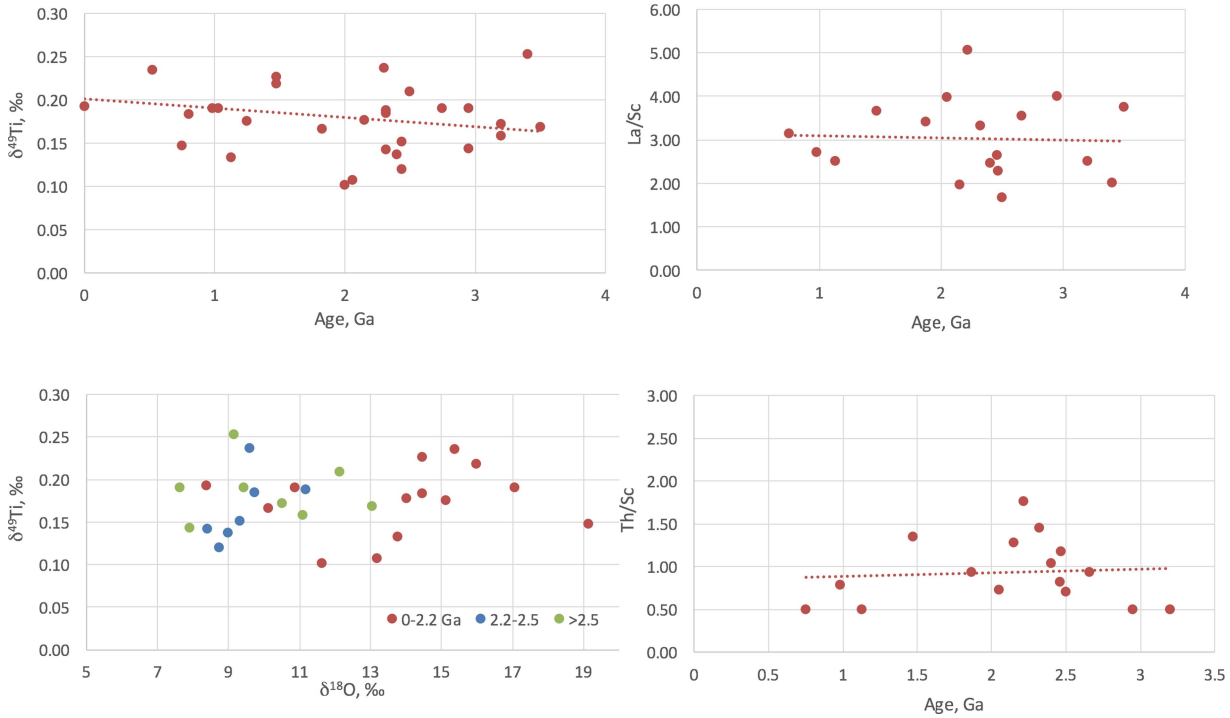

Extended Data Fig. 1 | Comparison of isotopic and key elemental ratios of the shales studied here, illustrating the relative constancy of the composition of the exposed crust that is undergoing weathering, and in particular proportion of exposed mafic versus silicic rocks. See, for example, refs [1,33]. The δ^{49}Ti data are from ref. [8], which used a large dataset that included many of the samples studied here. The elemental data are from Extended Data Table 3 and ref. [14]. Variation in the composition of the exposed crust cannot explain the oxygen-isotope trends that we have identified here.

33. McLennan, S. M., Hemming, S., McDaniel, D. K. & Hanson, G. N. Geochemical approaches to sedimentation, provenance and tectonics. *Geol. Soc. Am. Spec. Pap.* **284**, 21–40 (1993).

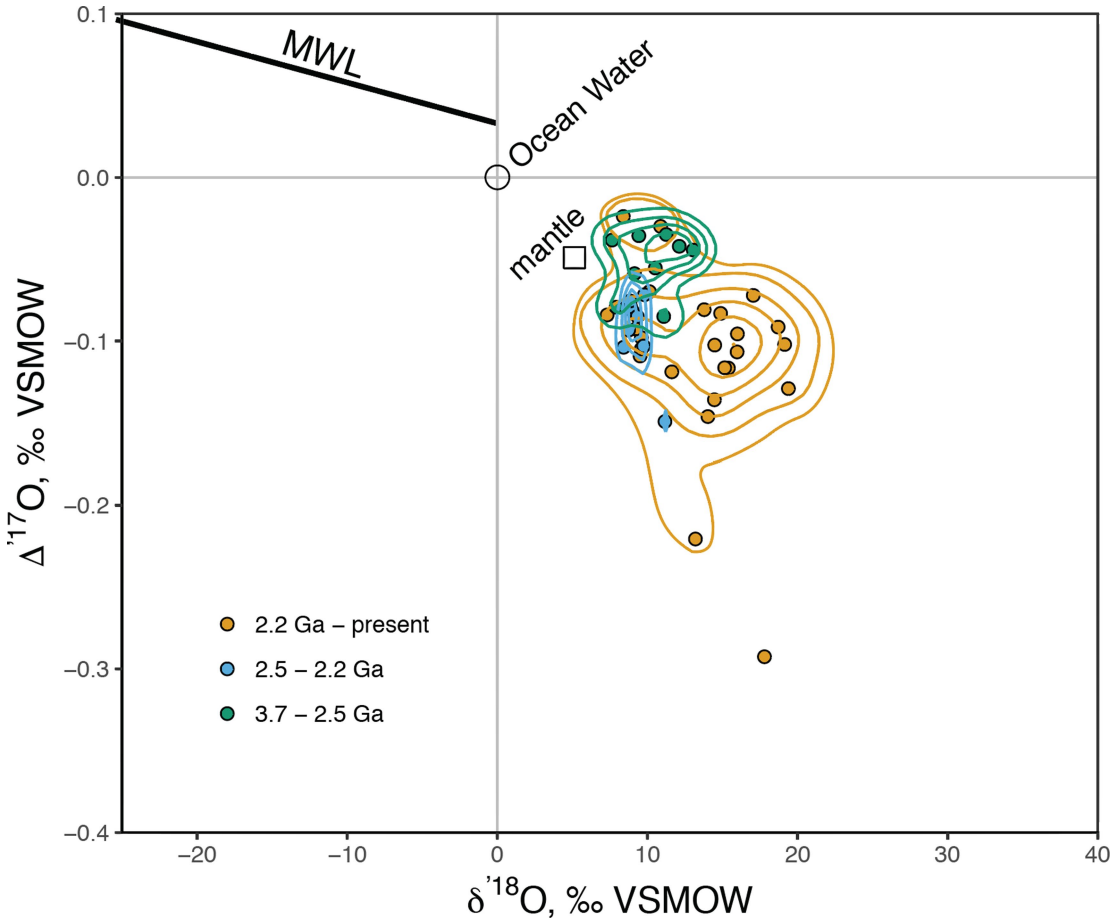

Extended Data Fig. 2 | Distribution density plot for the samples studied here. Data from Fig. 1.

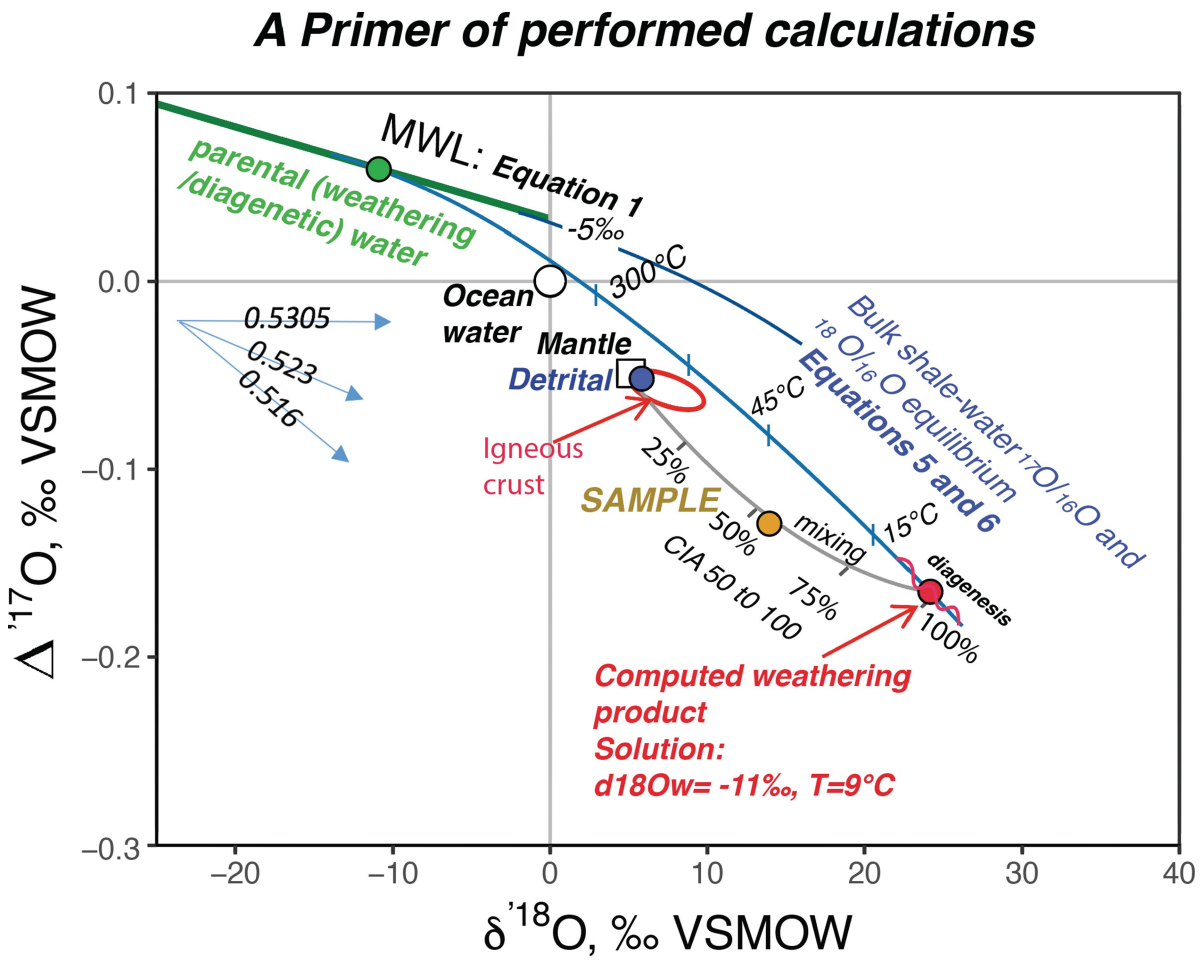

Extended Data Fig. 3 | Calculating the $\delta'^{18}O$ and $\Delta'^{17}O$ values of the weathering products of shales. Solving a system of three unknowns (for example, the temperature of alteration and the values of $\Delta'^{17}O$ and $\delta'^{18}O$ along the MWL) in three equations (Supplementary Information equations (1), (5) and (6)) follows these steps: the results of Supplementary Information equations (1), (5) and (6) are substituted sequentially into each other until one unknown is left. This results in a function with respect to temperature (T, a single parameter) to solve: $y = 0 = 36.323T - 23.33T^2 + 0.00264T^3 - 1.38 \times 10^7$. This is a third-order polynomial equation that has three roots; we solve for roots in a realistic temperature range to obtain the temperature and $\delta^{18}O_W$. The concave blue curve originating from a point on the MWL shows isotope fractionation between shale and water with the indicated temperatures of equilibration. The grey curve represents a mixing line between detrital and weathering products of the indicated proportions, computed using the CIA.

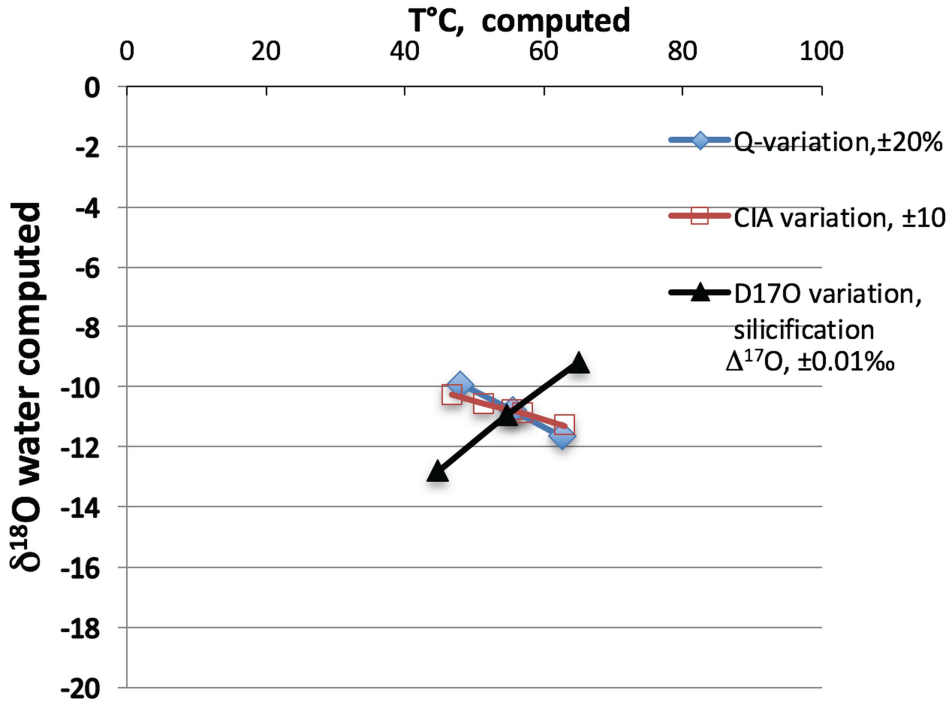

Extended Data Fig. 4 | Evaluating the sensitivity of reconstructed $\delta^{18}O_W$ and temperature values to variations in the input parameters. We show here the effects of varying the proportion of quartz (Q) in shales (±20%), the CIA (±10 units), and $\Delta'^{17}O$ (D170) (±0.01‰), the latter occurring naturally owing to, for instance, silicification.

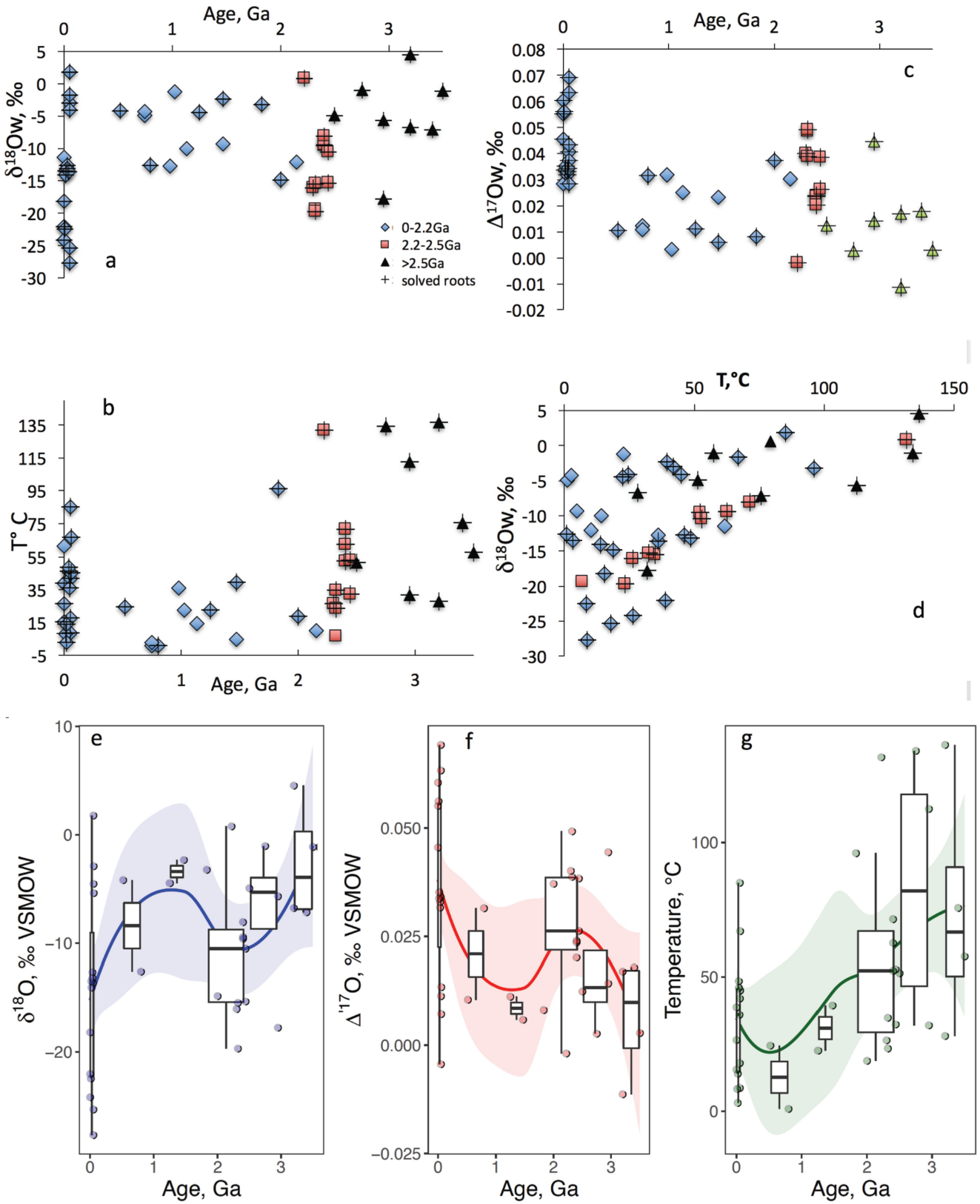

Extended Data Fig. 5 | See next page for caption.

Extended Data Fig. 5 | Calculated temperature, $\delta^{18}O_W$ and $\Delta^{17}O_W$ values plotted against age of shales. **a**, $\delta^{18}O_W$ versus age; **b**, temperature versus age; **c**, $\Delta^{17}O_W$ versus age; **d**, $\delta^{18}O_W$ versus temperature. These values are based on the solution of three equations with three input parameters: $\delta'^{18}O_{shale}$, $\delta'^{17}O_{shale}$ and the proportion of quartz (see Extended Data Fig. 3). Sensitivity analysis is provided in Extended Data Fig. 4. Most measurements yielded solved roots (plus signs within symbols); when equations could not be solved, small variations in the input parameters (Extended Data Table 1) allowed us to find roots. In particular, correcting for secondary silicification (see Extended Data Table 1) by decreasing $\Delta'^{17}O_{shale}$ by 0.01‰ to 0.08‰ along the silicification line allowed us to find roots in all but two cases. Note that the overall calculated $\delta^{18}O_W$ and temperature ranges agree with modern and recent values for surface, diagenetic, basinal and pore waters measured in drillholes[21]. Note also that the absolute calculated values for the temperature of water–rock interaction (weathering) and $\delta^{18}O_W$ depend on the assumed isotopic fractionations in Extended Data Fig. 6; however, given that these values solved within realistic bounds, the fractionations of ref. [19] and the MWL defined in ref. [17] are probably well constrained and calibrated in absolute triple-oxygen-isotope space. The lowest $\delta^{18}O_W$ and temperature are computed for recent clay samples from Antarctica, and for 2.5–2.2-Gyr-old synglacial Palaeoproterozoic shales, confirming the participation of low-$\delta^{18}O_w$ synglacial waters in diagenesis, as proposed previously[14]. The highest recent temperature and $\delta^{18}O_W$ values are for Palaeocene–Eocene (55-million-year-old) thermal maximum shales (ref. [34] and Extended Data Table 1). **e**–**g**, Interquartile range statistics and running averages for the parameters computed in **a**–**d**.

34. Frieling, J. et al. Paleocene–Eocene warming and biotic response in the epicontinental West Siberian Sea. *Geology* **42**, 767–770 (2014).

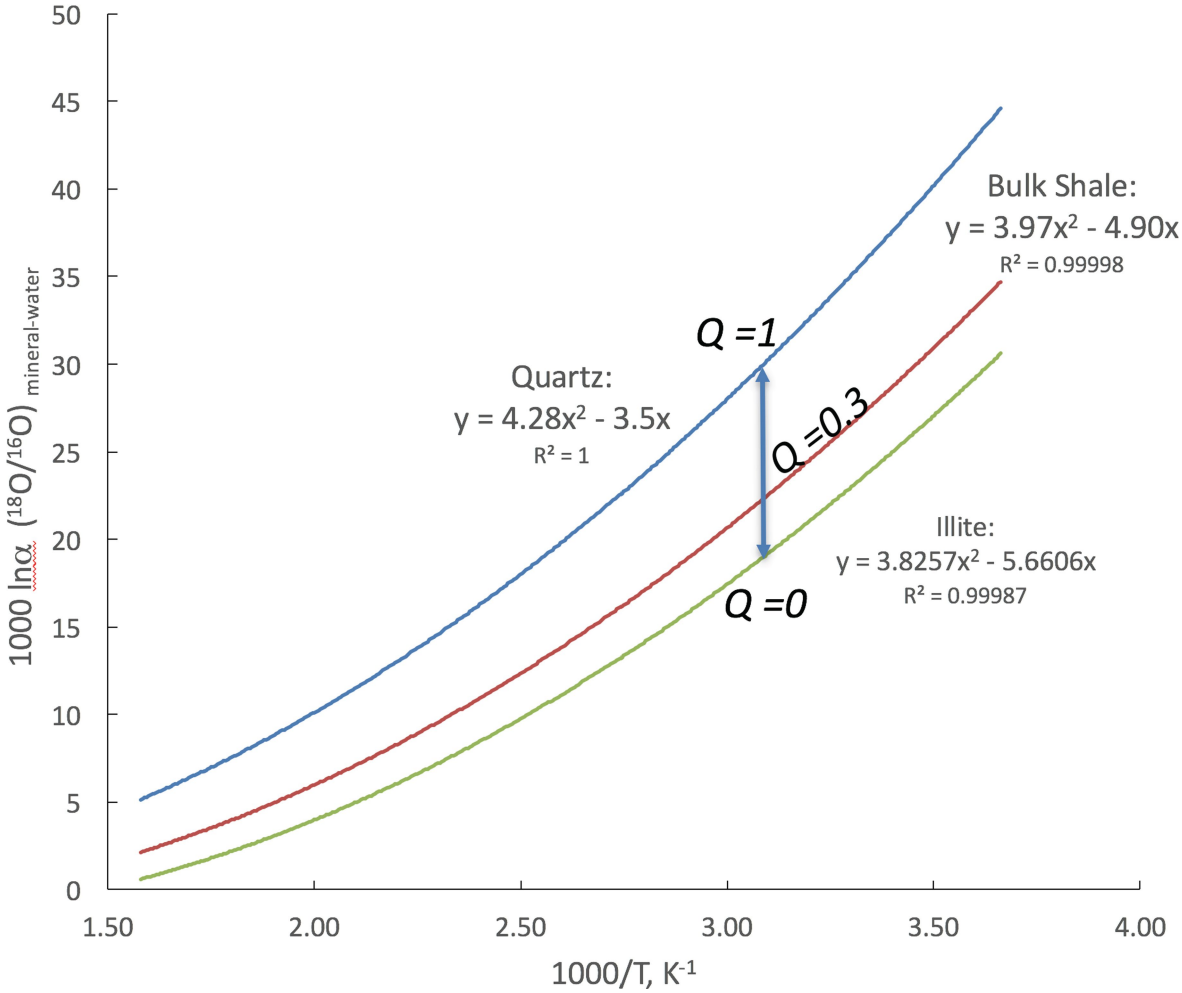

Extended Data Fig. 6 | Quartz/water, illite/water and bulk-shale/water $^{18}O/^{16}O$ fractionation factors. The quartz/water and illite/water 1,000lnα ($^{18}O/^{16}O$) fractionation factors are based on refs [19,35]. The bulk-shale/water 1,000lnα ($^{18}O/^{16}O$) fractionation factors are based on the assumption that bulk shale comprises 70% illite and 30% quartz (that is, Q = 0.3). The blue line (for quartz/water fractionation) corresponds to Supplementary Information equation (2) and equation (9) in ref. [19]. The green line (for illite/water fractionation) is the best-fit second-order polynomial with two fit coefficients based on the equation in ref. [35] that includes three fit coefficients. We used these coefficients to solve equations for bulk-shale/water triple-oxygen-isotope fractionations according to the proportion of quartz (determined through X-ray-diffraction; Extended Data Table 2).

35. Zheng, Y. F. Calculation of oxygen isotope fractionation in hydroxyl-bearing silicates. *Earth Planet. Sci. Lett.* **120**, 247–263 (1993).

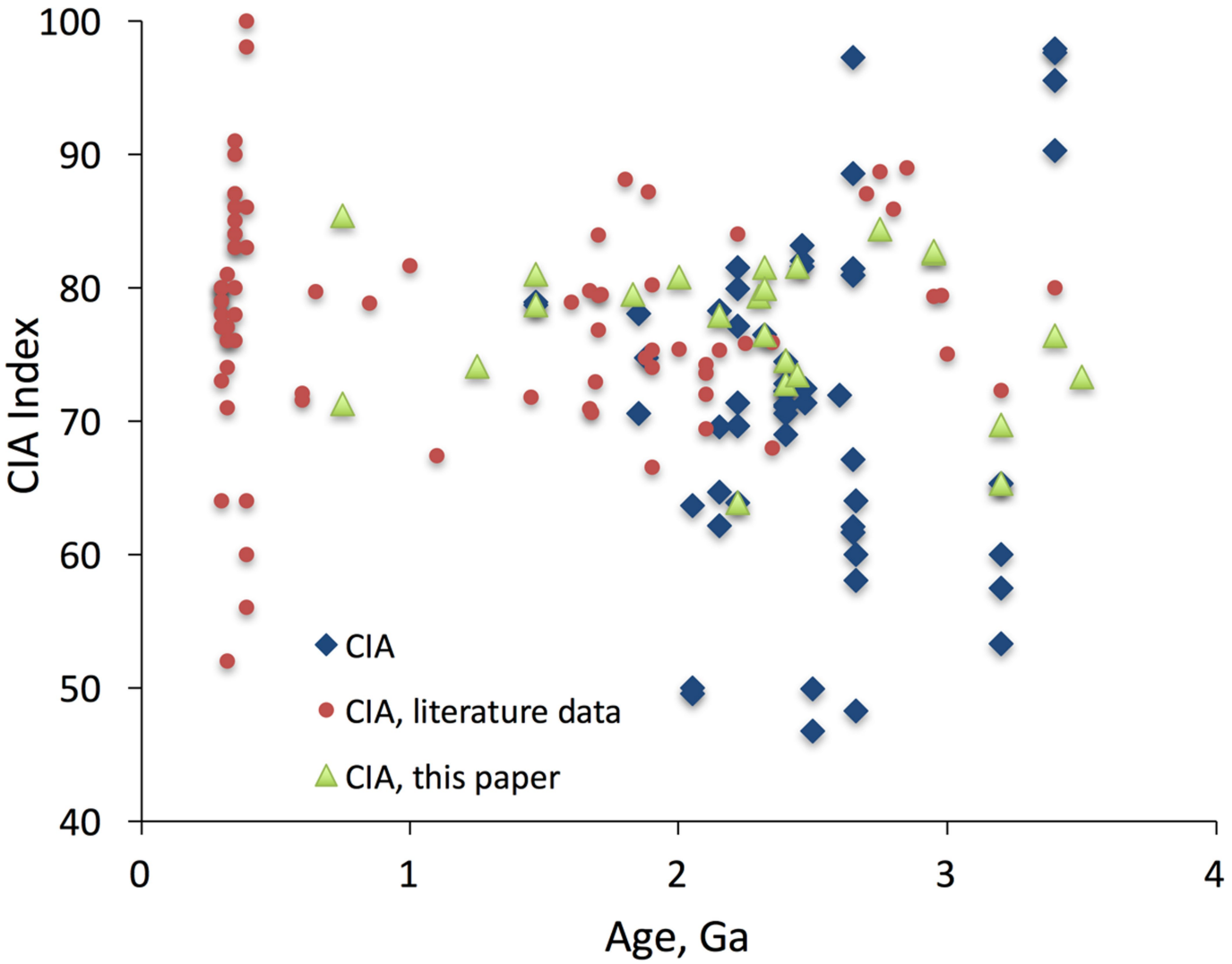

Extended Data Fig. 7 | Chemical index of alteration (CIA) plotted against time. $CIA = Al_2O_3/(Al_2O_3 + CaO + Na_2O + K_2O)_{mol}$. Data are taken from this work (triangles), ref. [14] (diamonds), and literature data (circles).

Extended Data Table 1 | Triple-oxygen-isotope analyses of the shale samples used here

	measured				linearized and normalized					Weathering product								Weathering waters		
AGE, Ga	$\delta^{17}O$, ‰, av	$\delta^{18}O$, ‰, av	$\Delta^{17}O$, ‰, av	±stdev	$\delta'^{17}O$, ‰, norm *	$\delta'^{18}O$, ‰, norm	$\Delta'^{17}O$, ‰, norm	n	CIA‡	$\delta^{18}O$ CIA corr ¶	$\Delta'^{17}O$ CIA corr	$\delta'^{17}O$ CIA corr	drillcore (d), outcrop (o)	Composite (cs), individual shale (is)	Sample size, n	Ref	Sample Description	$\delta^{49}Ti$ †	Quartz	T, °C	$\delta^{18}Ow$, ‰	$\delta^{17}Ow$ ‰	$\Delta^{17}Ow$ ‰
0	4.269	8.238	-0.101	0.022	4.426	8.387	-0.024	2	75	9.775	0.022	5.208	d	cs	18	36	Carribean Sea, Core 34 of Swedish Deep Sea Expedition 1947, secondary carbonate present	0.192	0.3	62	-11.4	-6.0	0.029
0	4.786	9.378	-0.189	0.011	4.940	9.518	-0.109	3	75	12.035	-0.148	6.236	o	is	1		Holocene silt, Oregon		0.3	15	-18.2	-9.6	0.046
0.00	1.155	2.480	-0.160	0.031	1.320	2.661	-0.091	3	100	2.661	-0.091	1.320	o	is	1		Suislaw River, Oregon clay +silt , river mud, Florence, Oregon		0.3	39	-22.0	-11.6	0.055
0.00	1.450	3.070	-0.177	0.002	1.615	3.249	-0.109	2	100	3.249	-0.109	1.615	o	is	1		Suislaw River, Oregon clay +silt , Florence, Oregon		0.3	27	-24.2	-12.8	0.060
0.05	0.030	0.376	-0.17	0.015	0.196	0.560	-0.101	2	100	0.560	-0.101	0.196	o	is	1	63	sample 2367, Antarctic claystone, Plio-Pleistocene, Transantarctic Mt, 85°S		0.01	18	-25.3	-13.4	0.063
0.05	0.030	0.405	-0.16	0.019	0.196	0.588	-0.116	5	100	0.588	-0.116	0.196	o	is	1	63	sample 2367, Antarctic claystone, Plio-Pleistocene, Transantarctic Mt, 85°S		0.01	9	-27.7	-14.6	0.069
0.01	9.775	19.053	-0.333	0.005	9.893	19.057	-0.217	3	100	19.057	-0.217	9.893	o	is	1	64	F108534_A, Late Miocene, Nevada, non-marine diatomite		0.99	8	-22.5	-11.9	0.056
0.018	15.533	30.112	-0.441	0.008	15.580	29.852	-0.257	3	100	29.852	-0.257	15.580	o	is	1	38	locality UO11095 Cabrillo Beach Museum parking lot, California: Valmonte Diatomite: middle Miocene		0.99	3	-13.5	-7.1	0.034
0.02	6.513	12.706	-0.228	0.012	6.657	12.809	-0.138	4	100	12.809	-0.138	6.657	o	is	1	39	R3888, kaolinite of lateritic profile, Long Reef Beach, near Deewhy, NSW, Australia: middle Miocene		0.01	14	-14.1	-7.4	0.035
0.035	3.634	7.150	-0.159	0.021	3.793	7.308	-0.084	3	100	7.308	-0.084	3.793	o	is	1		John Day fossil beds, Oregon, kaolinite. Oligocene		0.01	46	-12.6	-6.7	0.032
0.035	4.836	9.452	-0.178	0.013	4.990	9.591	-0.098	3	100	9.591	-0.098	4.990	o	is	1		John Day fossil beds, Oregon, smectite, Oligocene		0.3	48	-13.2	-6.9	0.033
0.045	4.647	9.084	-0.172	0.007	4.802	9.227	-0.093	3	74.0	11.640	-0.117	6.058	o	cs	7	40	Tyee Fm, Triangle Lake area, Oregon Coastal Ranges		0.3	36	-13.6	-7.2	0.034
0.051	9.739	18.709	-0.186	0.017	9.839	18.720	-0.091	4	100	18.720	-0.091	9.839	d	is	1	34	Russkaya Polyana Fm, claystone, W Siberia, Omsk Region, well 10, EECO excursion layer, depth 195m		0.3	85	1.8	0.9	-0.004
0.052	10.060	19.391	-0.227	0.016	10.157	19.389	-0.129	3	100	19.389	-0.129	10.157	d	is	1	34	Russkaya Polyana Fm, claystone, W Siberia, Omsk Region, well 10, EECO excursion layer, depth 198m		0.3	42	-4.5	-2.4	0.011
0.055	7.689	14.798	-0.161	0.027	7.804	14.873	-0.083	4	100	14.873	-0.083	7.807	d	is	1	34	Lulinvor Formation, W Siberia, Omsk region, well 10, PETM excursion claystone layer depth 236.85		0.3	67	-2.9	-1.5	0.007
0.056	8.314	15.930	-0.137	0.016	8.375	15.988	-0.107	3	100	15.988	-0.107	8.375	d	is	1	34	Lulinvor Formation, W Siberia, Omsk region, well 10, PETM excursion claystone layer depth 236.9		0.3	45	-5.4	-2.8	0.013
0.52	7.908	15.312	-0.215	0.007	8.042	15.380	-0.117	3	75	23.759	-0.163	12.441	o	cs	2	41	Poleta Formation, Poleta Folds, Eastern California, USA	0.235	0.3	24	-4.2	-2.2	0.010
0.75	9.022	17.767	-0.403	0.005	9.148	17.795	-0.293	3	85.4	22.247	-0.385	11.417	o	cs	12	42	Cerro Espuelitas Formation, Arroyo Del Soldado Group, Uruguay, numeric age tentative	0.318	0.3				no roots
0.8	7.400	14.385	-0.231	0.014	7.538	14.466	-0.1359	3	75.0	21.932	-0.202	11.433	d	cs	16	43,44,14	Wynniatt Fm, Shaler Supergroup, Victoria Island, N Canada, GNME drill core 07-04, sec. carbonate present	0.184	0.3	1	-12.6	-6.7	0.032
0.75	9.937	19.140	-0.217	0.024	10.053	19.143	-0.102	2	71.3	35.504	-0.145	18.690	d	cs	13	14, 44	Mwashya Subgroup, Upper Roan Group, Katanga Supergroup, Zambia, Drillhole RCB1, below glacials	0.147	0.3	1	-4.9	-2.6	0.012
0.98	5.589	10.748	-0.113	0.014	5.739	10.874	-0.030	2	75	14.748	0.010	7.834	o	cs	8	45,46,14	Upper part of the Ui Group, Lakhanda Series, Uchur-Maya Region, Siberia, Russia	0.190	0.3	36	-12.7	-6.7	0.032
1.025	8.852	17.021	-0.177	0.012	8.979	17.061	-0.072	2	75	27.122	-0.074	14.314	o	cs	5	45,46,14	Neryuen Formation, Lakhanda Series, Uchur-Maya Region, Siberia, Russia	0.190	0.3	23	-1.2	-0.6	0.003
1.13	7.086	13.684	-0.173	0.009	7.227	13.775	-0.081	2	75	20.550	-0.092	10.810	o	cs	12	14, 37	Bylot Supergroup, northern Baffin and Bylot Islands, Canada, secondary carbonate present	0.133	0.3	14	-10.0	-5.3	0.025
1.25	7.774	15.058	-0.214	0.020	7.910	15.129	-0.116	8	74.0	23.936	-0.167	12.532	o	cs	18	47,45,14	Totta, Talyn, Trekhgornaya and Dim formations, Uchur-Maya Region, Yudoma-Maya trough, Siberia, Russia	0.175	0.3	23	-4.5	-2.4	0.011
1.47	8.260	15.940	-0.197	0.022	8.391	15.998	-0.096	2	81.2	21.420	-0.111	11.252	d	cs	14	14	Newland Formation, Lower Belt Supergroup, Montana, USA, drill core SC-93	0.218	0.11	5	-9.3	-4.9	0.023
1.47	7.441	14.398	-0.198	0.0048	7.579	14.479	-0.102	4	78.7	20.039	-0.127	10.504	d	is	1	14	SC93-1906, Newland Fm, Lower Belt Supergroup, Montana, drill core SC-93, depth 1906, studied by XRD	0.226	0.11	39	-2.3	-1.2	0.006
1.83	5.148	9.988	-0.151	0.021	5.300	10.122	-0.070	2	79.5	12.292	-0.070	6.451	d	cs	11	48, 14	Rove Formation, near Thunder Bay, Ontario, Canada, drill core 89-MC-1	0.166	0.3	96	-3.2	-1.7	0.008
2.0	5.905	11.517	-0.205	0.012	6.053	11.634	-0.119	2	80.8	14.523	-0.149	7.556	d	cs	10	49, 14	Maraloou Formation, southeastern Capricorn Orogen, Australia, drill core KDD1	0.101	0.3	19	-14.8	-7.8	0.037
2.06	6.636	13.098	-0.312	0.009	6.780	13.196	-0.221	4	64.0	29.129	-0.609	14.844	d	cs	14	51	Zaonega Formation, Lower Ludikovian Series, Karelia, Russia, drill cores 175 and 5190	0.107	0.3				no roots
2.15	7.152	13.934	-0.240	0.006	7.292	14.022	-0.146	3	77.9	19.583	-0.206	10.182	d	cs	20	51, 14	Sengoma Argillite Formation, Pretoria Group, Lobatse, Botswana, drill core STRAT 2	0.177	0.3	10	-12.1	-6.4	0.030
2.30	4.830	9.453	-0.185	0.018	4.984	9.592	-0.105	4	79.3	11.424	-0.130	5.931	d	cs	10	51,52,14	Timeball Hill Fm, Lower Pretoria Group, Transvaal Basin, S Africa, drill cores EBA-1 and 2, above all glacials	0.237	0.3	26	-16.0	-8.5	0.040
2.22	4.977	9.668	-0.152	0.0065	5.130	9.805	-0.072	5	63.9	17.128	-0.077	9.010	d	is	1	14	EBA-1 569.2 drillhole EBA-1, individual sample from depth 569.2, studied by XRD		0.86	132	0.8	0.4	-0.002
2.32	4.910	9.601	-0.184	0.015	5.063	9.738	-0.103	2	81.5	11.352	-0.122	5.900	d	is	1	14	EBA-1 1093 m, Lower Timeball Hill Fm, S Africa; immediately above Huronian glacials, studied by XRD	0.184	0.41	35	-15.5	-8.2	0.039
2.32	5.633	11.059	-0.234	0.023	5.783	11.182	-0.149	2	79.9	13.984	-0.202	7.216	d	is	1	14	EBA-1 1151.7m, Lower Timeball Hill Fm, S Africa; immediately above Huronian glacials. studied by XRD	0.188	0.35	7	-19.4	-10.2	0.049
2.32	4.203	8.264	-0.181	0.002	4.359	8.413	-0.104	2	76.4	9.675	-0.134	4.998	d	is	1	14, 52	H-68-3, 3410m, Eplett drillhole, Gowganda Fm, ON, Canada, above all Huronian glacials, studied for XRD	0.142	0.395	23	-19.7	-10.4	0.049
2.4	4.535	8.850	-0.160	0.003	4.690	8.994	-0.082	2	72.8	11.370	-0.095	5.936	d	is	1	14, 12	Drillcore A-77-10, 441 m, Pecors Fm (379-678'), L Huronian Supergroup, ON, Canada, studied by XRD	0.137	0.203	52	-9.6	-5.1	0.024
2.4	4.469	8.720	-0.157	0.015	4.625	8.866	-0.079	4	74.5	10.809	-0.088	5.646	d	is	1	14	Drillcore 150-4, 4912 m, Pecors Fm, L Huronian Supergroup, Canada, above the oldest Huronian glacial		0.3	63	-9.4	-5.0	0.024
2.4	4.468	8.712	-0.154	0.018	4.624	8.858	-0.075	14	74.5	10.792	-0.081	5.644	d	is	1	14	Drillcore 150-4, Pecors Fm, Lower Huronian Supergroup, Canada, above the oldest Huronian glacial		0.3	71	-8.0	-4.2	0.020
2.44	4.705	9.179	-0.163	0.020	4.860	9.321	-0.085	8	81.6	10.678	-0.094	5.570	d	is	1	14, 12	Drillcore DD04, 98.8m, Turee Creek Fm, Hamersley, W Australia, above oldest glacial, studied by XRD	0.151	0.23	53	-10.5	-5.5	0.026
2.44	4.393	8.603	-0.171	0.001	4.549	8.750	-0.093	2	73.4	10.739	-0.120	5.577	d	cs	10	14, 12	Pecors and McKim Fm, L Huronian, Canada, drill cores A-77-10, A-77-9 ,143-4,150-4, below all glacials	0.120	0.3	32	-15.3	-8.1	0.038
2.5	6.250	12.024	-0.129	0.003	6.396	12.136	-0.042	2	75	17.271	-0.014	9.148	d	cs	12	14, 53	Mt McRae Shale, Hamersley Basin, W Australia, drillcores WLT-02, WLT-10, secondary carbonate present	0.209	0.3	51	-4.9	-2.6	0.012
2.75	4.819	9.300	-0.115	0.018	4.973	9.441	-0.036	2	84.4	10.553	-0.020	5.578	d	cs	16	14, 53	Manjeri Fm, Bubi and Gweru Greenstone Belts, Zimbabwe, drillcores 690B92-02,696C92-01,711B93-02	0.191	0.3	134	-1.0	-0.5	0.003
2.95	3.960	7.757	-0.156	0.034	4.117	7.911	-0.079	3	82.6	8.397	-0.084	4.370	d	cs	3	55	Monzaan Group, Pongola Supergroup, South Africa, drillcore	0.143	0.3	32	-17.8	-9.4	0.044
2.95	3.860	7.491	-0.114	0.011	4.018	7.646	-0.038	4	82.7	7.988	-0.021	4.217	o	is	1	14,56,57	DRB-3 , W Rand Group, Government Subgroup, Witwatersrand Supergroup, S Africa, sample from mine	0.190	0.3	113	-5.7	-3.0	0.014
3.2	5.376	10.393	-0.138	0.014	5.527	10.523	-0.055	3	69.7	15.943	-0.033	8.425	d	cs	13	14, 58	Clutha Fm, Moodies Group, Barberton Greenstone Belt, S Africa, short drillcles, few % secondary silicification	0.172	0.3	136	4.5	2.4	-0.011
3.20	5.643	10.955	-0.156	0.015	5.793	11.079	-0.085	3	65.3	20.306	-0.119	10.653	d	is	1	14, 58	Drillcore 28-148, 43.3m, Clutha Fm, Moodies Gp, Barberton Greenstone Belt, S Africa, some sec. silicification	0.158	0.3	28	-6.8	-3.6	0.017
3.40	4.640	9.007	-0.138	0.011	4.795	9.150	-0.059	3	76.4	11.072	-0.049	5.825	o	is	1	14, 59	KS-1 , Kromberg Fm Onverwacht Group, Barberton Greenstone Belt, South Africa, minor sec. silicification	0.253	0.3	76	-7.1	-3.8	0.018
3.5	6.737	12.952	-0.134	0.006	6.880	13.052	-0.044	2	73.3	19.987	-0.015	10.588	o	cs	7	14, 60	Daitari Greenstone Belt, India, uncertain age, probably 3.5 Ga, some secondary silicification	0.168	0.3	58	-1.1	-0.6	0.003
3.75	5.779	11.117	-0.119	0.006	5.928	11.239	-0.035	3	75	15.479	0.001	8.212	o	is	1	61	sample R5310 , chloritized siltstone, surface outcrop, Isua greenstone belt, Greenland		0.01	79	0.6	0.3	-0.002
3.80	3.172	6.150	-0.091	0.014	3.333	6.315	-0.017	3	65.3	4.765	0.102	2.630	o	gr		62	Chinese granite -mylonitized, oldest rock in China 3.8Ga						
mantle	2.545	5.003	-0.121	0.034	2.677	5.140	-0.049										SCO average (n=12)						
mantle	2.681	5.153	-0.053	0.007	-	-	-										SCO analyzed by Pack et al., 2016 Rapid Comm Mass Spectrometry, 30, 1495.						
mantle	2.690	5.280	-0.101	0.015													SCO analyzed Pack and Herwartz, 2014 , EPSL 390, 138.						

Details of the shale samples are taken from refs [12,14,36–64].

*Normalized to the mantle value, −0.05‰ $\Delta^{17}O$.

†Data from ref. [8].

‡CIA is calculated using X-ray fluorescence (XRF) analysis of rocks where available. A generically average CIA of 75 is assumed for samples without chemical analysis or for which inductively coupled plasma mass spectrometry (ICPMS) analysis shows the calcium carbonate content to be greater than 5 wt% (most likely because of to secondary carbonate). A CIA of 100 is assumed for samples of 100% clay.

¶Corrected using the $\delta'^{18}O$ and $\Delta'^{17}O$ values of igneous crust, namely 7‰ and −0.07‰ respectively.

36. Ovey, C. D. Preliminary results from the study of an ocean core obtained by the Swedish Deep-Sea Expedition, 1947-48. *J. Glaciol.* **1**, 370–373 (1950).
37. Kah, L. C. et al. $\delta^{13}C$ stratigraphy of the Proterozoic Bylot Supergroup, Baffin Island, Canada: implications for regional lithostratigraphic correlations. *Can. J. Earth Sci.* **36**, 313–332 (1999).
38. Campbell, A. S. & Clark, B. L. Miocene radiolarian faunas from southern California. *Geol. Soc. Am. Spec. Pap.* **51**, 1–78 (1944).
39. Retallack, G. J. Lateritization and bauxitization events. *Econ. Geol.* **105**, 665–667 (2010).
40. Ryu, I.-C. Petrography, diagenesis and provenance of Eocene Tyee Basin sandstones, southern Oregon Coast Range: new view from sequence stratigraphy. *Isl. Arc* **12**, 398–410 (2003).
41. McKee, E. H. & Gangloff, R. A. Stratigraphic distribution of archaeocyathids in the Silver Peak Range and the White and Inyo Mountains, western Nevada and eastern California. *J. Paleontol.* **43**, 716–726 (1969).
42. Pecoits, E. et al. U–Pb detrital zircon ages from some Neoproterozoic successions of Uruguay: provenance, stratigraphy and tectonic evolution. *J. S. Am. Earth Sci.* **71**, 108–130 (2016).
43. Thomson, D., Rainbird, R. H., Planavsky, N., Lyons, T. W. & Bekker, A. Chemostratigraphy of the Shaler Supergroup, Victoria Island, NW Canada: a record of ocean composition prior to the Cryogenian glaciations. *Precambr. Res.* **263**, 232–245 (2015).
44. Key, R. M. et al. The western arm of the Lufilian Arc in NW Zambia and its potential for copper mineralization. *J. Afr. Earth Sci.* **33**, 503–528 (2001).
45. Podkovyrov, V. N. et al. Provenance and source rocks of Riphean sandstones in the Uchur-Maya region (east Siberia): implications of geochemical data and Sm-Nd isotopic systematics. *Stratigr. Geol. Correl.* **15**, 41–56 (2007).
46. Cullers, R. L. & Podkovyrov, V. N. The source and origin of terrigenous sedimentary rocks in the Mesoproterozoic Ui group, southeastern Russia. *Precambr. Res.* **117**, 157–183 (2002).
47. Vinogradov, V. I., Veis, A. F., Bujakaite, M. I. & Golovin, D. I. Isotopic evidences of epigenetic transformations and the problem of the age of Precambrian rocks in the Yudoma-Maya trough, eastern Siberia. *Lithol. Miner. Resour.* **35**, 141–152 (2000).
48. Addison, W. D., Brumpton, G. R., Davis, D. W., Fralick, P. W. & Kissin, S. A. Debrisites from the Sudbury impact event in Ontario, north of Lake Superior, and a new age constraint: are they base-surge deposits or tsunami deposits? *Geol. Soc. Am. Spec. Pap.* **465**, 245–268 (2010).
49. Sheppard, S. et al. A new Paleoproterozoic tectonic history of the eastern Capricorn Orogen, Western Australia, revealed by U-Pb zircon dating of micro-tuffs. *Precambr. Res.* **286**, 1–19 (2016).
50. Kipp, M. A., Stüeken, E. E., Bekker, A. & Buick, R. Selenium isotopes record extensive marine suboxia during the Great Oxidation Event. *Proc. Natl Acad. Sci. USA* **114**, 875–880 (2017).
51. Rouxel, O. J., Bekker, A. & Edwards, K. J. Iron isotope constraints on the Archean and Paleoproterozoic ocean redox state. *Science* **307**, 1088–1091 (2005).
52. Rasmussen, B., Bekker, A. & Fletcher, I. R. Correlation of Paleoproterozoic glaciations based on U–Pb zircon ages for tuff beds in the Transvaal and Huronian Supergroups. *Earth Planet. Sci. Lett.* **382**, 173–180 (2013).
53. Rasmussen, B., Blake, T. S. & Fletcher, I. R. U–Pb zircon age constraints on the Hamersley spherule beds: evidence for a single 2.63 Ga Jeerinah-Carawine impact ejecta layer. *Geology* **33**, 725–728 (2005).
54. Hofmann, A., Bolhar, R., Dirks, P. & Jelsma, H. The geochemistry of Archaean shales derived from a mafic volcanic sequence, Belingwe greenstone belt, Zimbabwe: provenance, source area unroofing and submarine versus subaerial weathering. *Geochim. Cosmochim. Acta* **67**, 421–440 (2003).
55. Planavsky, N. J. et al. Evidence for oxygenic photosynthesis half a billion years before the Great Oxidation Event. *Nat. Geosci.* **7**, 283–286 (2014).
56. Kositcin, N. & Krapež, B. Relationship between detrital zircon age-spectra and the tectonic evolution of the Late Archaean Witwatersrand Basin, South Africa. *Precambr. Res.* **129**, 141–168 (2004).
57. Armstrong, R. A., Compston, W., Retief, E. A., Williams, I. S. & Welke, H. J. Zircon ion microprobe studies bearing on the age and evolution of the Witwatersrand triad. *Precambr. Res.* **53**, 243–266 (1991).
58. Javaux, E. J., Marshall, C. P. & Bekker, A. Organic-walled microfossils in 3.2-billion-year-old shallow-marine siliciclastic deposits. *Nature* **463**, 934–938 (2010).
59. Byerly, G. R., Kröner, A., Lowe, D. R. & Todt, W. Prolonged magmatism and time constraints for sediment deposition in the early Archean Barberton greenstone belt: evidence from the Upper Onverwacht and Fig Tree groups. *Precambr. Res.* **78**, 125–138 (1996).
60. Mukhopadhyay, J. et al. Dating the oldest greenstone in India: a 3.51-Ga precise U-Pb SHRIMP zircon age for dacitic lava of the Southern Iron Ore Group, Singhbhum Craton. *J. Geol.* **116**, 449–461 (2008).
61. Myers, J. S. Protoliths of the 3.8–3.7 Ga Isua greenstone belt, West Greenland. *Precambr. Res.* **105**, 129–141 (2001).

62. Liu, D. Y., Nutman, A. P., Compston, W., Wu, J. S. & Shen, Q. H. Remnants of ≥3800 Ma crust in the Chinese part of the Sino-Korean craton. *Geology* **20**, 339–342 (1992).
63. Retallack, G. J. & Krull, E. S. Neogene paleosols in the Sirius Group, Dominion, Antarctica. *US Antarctic J.* **30**, 10–14 (1997).
64. Bell, M. A. & Haglund, T. R. Fine-scale temporal variation of the Miocene stickleback *Gasterosteus doryssus*. *Paleobiology* **8**, 282–292 (1982).

Extended Data Table 2 | Quantitative XRD data for a selection of studied shales

Sample	Age, Ga	SiO_2 norm	CIA	$\delta^{18}O$, ‰* published	$\delta^{18}O$, ‰, new	$\Delta^{17}O$, ‰, av	Quartz, %	s.d	Tot Mica, %	Albite, %	s.d	Total	Other
SC-93_1906	1.47	**64.00**	78.7	14.30	14.40	-0.198	10.6 ±	2.9	88.4	±		99.0	
EBA-1_569.2	2.22	**86.30**	63.9	9.50	9.67	-0.152	70.1 ±	4.3	11	14.4 ±	1.2	95.5	
EBA-1_1093	2.32	**61.00**	81.5	10.10	9.60	-0.184	38.5 ±	2.5	55.9	±		94.4	Amphibole (5.7%)
EBA-1_1151.7	2.32	**66.90**	79.9	11.74	11.06	-0.234	32.5 ±	1.5	60.6	±		93.1	Amphibole (5.7%)
H-68-3_3410	2.32	**60.10**	76.4	8.34	8.26	-0.181	38.3 ±	1.2	58.7	3 ±	0.4	100.0	
A-77-10_441	2.40	**59.00**	72.8	9.47	8.85	-0.160	20.3 ±	2.3	74	5.0 ±	1.1	99.3	
DD04_98.8	2.46	**61.50**	81.6	8.52	9.18	-0.163	22.2 ±	1.0	74.3	3.3 ±	0.3	99.8	
89-MC-1_795	1.85	**61.50**	70.5	14.50			23.8 ±	1.3	62.9	10.3 ±	1.0	97.0	
EBA-1_574.7	2.32	**66.00**	71.3	7.79			40.6 ±	2.8	49.3	10.1 ±	6	100.0	
EBA-1_803.7	2.32	**63.10**	77.1	7.37			38.8 ±	1	61.2	±		100.0	
DD04_112.5	2.47	**58.80**	82.0	9.22			23.8 ±	0.6	76	0.3 ±	0	100.1	

*Run as CO_2 for $\delta^{18}O$ only; previously published[14].

Extended Data Table 3 | New XRF analyses of samples studied here

	Daitari Greenstone Belt, India			W Rand Group, Witwatersrand Supergroup S Africa	Barberton Greenstone Belt, Onverwacht Group, Kromberg Formation, South Africa	Bylot Supergroup, northern Baffin and Bylot Islands, Canada				Mwashya Subgroup, Upper Roan Group, Zambia					
Sample	DM 23	DM14	DM2	DRB3	KS-1	JD79 183B	JD79 297-1	JD79 I29 I-1	JD79	MJ 37	MJ 39	MJ 40	MJ 43	MJ 49	MJ
core/outcrop	o	o	o	mine	o	o	o	o	c	c	c	c	c	c	c
Age	3.5	3.5	3.5	2.95	3.40	1.27	1.27	1.27	1.13	0.75	0.75	0.75	0.75	0.75	0.75
n	1	1	1	1	1	1	1	1	3	1	1	1	1	1	4
SiO2	92.65	96.72	74.54	72.40	75.19	61.76	67.41	74.74	67.97	61.58	64.90	59.81	61.17	59.78	61.45
TiO2	0.16	0.08	0.74	0.46	0.75	0.63	1.47	0.67	0.92	1.69	1.21	0.83	1.10	1.51	1.27
Al2O3	5.17	1.77	16.80	11.43	16.96	12.77	18.38	15.33	15.50	16.76	17.81	19.15	11.50	14.74	15.99
Fe2O3	0.23	0.42	2.43	9.96	1.84	4.47	3.42	4.58	4.15	10.14	7.62	14.20	17.54	8.67	11.63
MnO	0.00	0.05	0.00	0.10	0.00	0.02	0.05	0.04	3.52	0.09	0.06	0.10	0.08	0.05	2.59
MgO	0.14	0.19	0.32	3.53	0.28	7.89	1.63	1.03	0.04	2.30	2.02	2.75	2.84	3.04	0.08
CaO	0.05	0.04	0.00	0.29	0.11	*5.47**	0.40	0.09	0.24	1.15	0.45	0.39	1.33	*5.03**	0.83
Na2O	0.00	0.10	0.00	0.00	0.00	1.72	3.08	0.05	1.62	2.70	2.18	0.26	1.85	3.16	2.03
K2O	1.53	0.54	5.00	1.61	4.65	4.84	3.89	3.25	3.99	3.24	3.43	2.27	2.33	3.57	2.97
P2O5	0.02	0.02	0.04	0.03	0.04	0.19	0.07	0.03	0.09	0.13	0.10	0.09	0.11	0.21	0.13
Total	99.96	99.94	99.87	99.81	99.82	94.29	99.79	99.80	97.96	99.78	99.78	99.85	99.85	94.75	98.80
CIA	74.74	69.60	75.60	82.70	76.60	*41.48*	65.14	81.62	62.75	63.16	69.40	85.18	59.83	*44.7*	64.46
ppm															
Rb	38	24	140	66	116	126	156	134	139	181	126	120	150	159	147
Sr			18	3	7	140	89	32	87	164	87	41	98	265	131
Ba	35		345	273	298	343	501	279	374	375	541	229	188	403	347
Zr	51	17	168	101	177	146	230	588	321	300	247	142	181	247	223
Y			17	12	13	14		25	19	30	33	10	22	29	25
Nb	9	6	13	10	11	14	42	18	24	52	44	22	30	37	37
Cs								4				27	18	4	
Sc	3	3	14	8	11	14	21	9	15	27	21	16	8	23	19
V	21	15	94	88	137	464	179	70	237	156	142	109	99	166	134
Cr	46	247	78	416	206	67	122	55	81	114	93	98	46	76	85
Ni	10	77	18	276	77	52	12	24	29	24	20	36		26	26
Cu		5		42	94	56		9	33		2	33	2	17	14
Zn		34	11	77	153	319	87	101	169	123	172	119	168	37	124
Ga	4		17	13	20	15	20	16	17	24	22	20	15	21	21
La	25		25	32	23	27	44	41	37	70	51	61	51	66	60
Ce	59	22	39	42	18	67	120	78	88	96	106	106	122	119	110
Pr	8	1	5	8	4	14	14	8	12	11	12	14	12	11	12
Nd	42		11	6		11	37	27	25	27	37	37	28	37	33
Hf					2										
Pb				1	18	5		31	18	13	1				7
Th				4		1		14	7	3	10			15	9
Ta									4						

Sample	Ui Fm Upper part of the Ui Group, Lakhanda Series, Uchur-Maya Region, Siberia, Russia	SC-93 Newland Formation, Lower Belt Supergroup Montana, USA	89MC Rove Formation, near Thunder Bay, Ontario, Canada	KDD Maraloo Formation, SE Capricorn Orogen, Australia	DH-51XX Zaonega Formation, lower Ludikovian Series, Karelia, Russia	STRAT-2 Sengoma Argillite Formation, Pretoria Series, Lobatse, Botswana	EBA-1 Upper Timeball Hill Fm, shale+siltstone, Potchefstroom Synclinorium, South Africa; above all glacials	EBA-1 and H-68 Eplett drillhole, Gowganda Formation, Huronian Supergroup, Cobalt area ON, Canada, above all Huronian glacials	A77 and 150 Pecors Formation (14'-292'), Lower Huronian Supergroup ON, Canada, above the oldest Huronian glacial	DD04 Turee Creek Group, Hamersley Province, Western Australia, above the oldest Huronian glacial	143/4 McKim Formation (2162-2550'), Lower Huronian Supergroup ON, Canada, below all glacials	WLT Mt McRae Shale, Hamersley Province, Western Australia	FVG Roy Hill Shale, Jeerinah Fm, Western Australia	Dominion Reef, South Africa	28 166 Clutha Formation, Moodies Group, Barberton Greenstone Belt, South Africa	Barberton Greenstone Belt, Onverwacht Group, Kromberg Formation, South Africa	DM, Daitari Greenstone Belt, India, slate
core/outcrop	o	c	c	c	c	c	c	c	c	c	c	c	c	c	c	o	o
Age	0.98	1.47	1.85	1.87	2.05	2.15	2.22	2.32	2.4	2.46	2.47	2.5	2.66	2.95	3.2	3.4	3.5
n	5	2	2	3	4	3	3	3	7	3	4	4	4	1	4	1	3
SiO2	59.96	63.7	56.2	64.34	64.13	66.12	70.53	64.54	58.22	60.05	58.26	46.18	64.29	72.40	60.83	75.19	74.54
TiO2	1.04	0.8	0.9	0.87	0.68	0.75	0.59	0.73	0.86	0.62	0.87	0.43	0.67	0.46	0.56	0.75	0.33
Al2O3	15.66	20.8	22.6	18.55	16.88	17.10	16.29	20.80	24.13	18.09	23.70	12.77	15.76	11.43	15.01	16.96	7.92
Fe2O3	9.96	8.2	7.0	7.21	4.20	6.11	6.07	6.71	5.67	9.90	6.20	4.39	6.10	9.96	7.84	1.84	1.03
MgO	2.45	1.3	2.8	3.74	2.40	2.84	1.09	1.64	2.31	7.36	2.09	10.29	3.40	3.53	5.08	0.28	0.22
MnO	0.05	0.0	0.0	0.63	0.05	0.02	0.02	0.20	0.04	0.04	0.04	0.41	0.08	0.10	0.17	0.00	0.02
CaO	0.41	0.1	0.4	0.41	2.77	0.97	0.70	0.59	0.25	0.16	0.22	3.56	1.40	0.29	*0.62*	0.11	0.03
K2O	1.88	4.7	5.4	3.03	1.08	3.60	3.56	3.77	7.52	3.46	7.58	7.67	7.11	0.00	5.44	0.00	0.03
Na2O	4.39	0.2	0.8	0.86	7.50	2.23	0.93	0.70	0.61	0.05	0.63	0.16	0.22	1.61	1.67	4.65	2.36
P2O5	0.46	0.1	0.1	0.10	0.09	0.11	0.09	0.14	0.11	0.12	0.12	0.08	0.08	0.03	0.10	0.04	0.03
Total	99.40	99.8	96.2	99.74	99.79	99.86	99.86	99.82	99.72	99.84	99.69	85.93	98.76	99.81	99.37	99.82	99.92
LOI		0.2	3.8	0.26	0.22	0.14	0.14	0.18	0.28	0.16	0.31	0.00	1.24		0.63		
CIA	74.80	78.8	74.3	76.49	56.60	65.45	70.48	77.07	71.95	82.22	70.82		60.72	82.70	*62.70*	76.60	73.31
ppm																	
Rb	193	129	225	148	37	184	183	181	329	140	320	224	151	66	142	116	67
Sr	29	71	87	36	202	88	84	89	44	9	36	60	32	3	247	7	18
Ba	563	337	1182	1805	662	857	422	626	1302	412	1151	377	406	273	712	298	190
Zr	246	230	159	137	123	164	176	157	146	138	156	108	247	101	121	177	78
Y		29	36	37	20	32	30	30	28	19	26	23	53	12	21	13	17
Nb	18	17	16	16	11	14	15	17	12	10	13	12	23	10	10	11	9
Sc	20	12	19	25	14	17	11	15	18	20	19	24	15	8	14	11	7
V		114	222	196	88	233	102	137	168	123	167	75	109	88	107	137	43
Cr	92	105	168	179	126	140	96	147	164	151	159	98	188	416	658	206	123
Ni		53	37	181	77	117	41	64	72	76	89	84	118	276	291	77	35
Cu		14	33	58	10	94	32	47	22	3	63	24	121	42	31	94	
Zn		49	163	187	55	170	94	102	64	70	56	355	96	77	84	153	22
Ga		25	31	24	20	24	20	26	31	24	30	17	25	13	19	20	11
La	54	42	53	95	55	34	53	51	43	52	43	39	54	32	35	23	25
Ce	89	88	108	200	119	74	116	110	91	93	88	85	119	42	68	18	40
Pr		9	11	21	13	9	13	13	9	11	9	11	11	8	7	4	5
Nd	37	41	40	62	39	23	52	45	37	43	39	26	51	6	23		26
Hf	7	7	7	5	4	5	6	6	5	5	5	4	6		3	2	
Pb		8	14	6		16	18	75	15	5	15	20	14	1	16	18	
Th	16	16	23	20	10	22	19	22	18	16	22	17	14	4	7		
Ta	6.15																

bdl, below detection limit; LOI, loss on ignition; p.p.m., parts per million.
*Secondary carbonate present.